

# Simulating anharmonic crystals: Lights and shadows of first-principle approaches

Lorenzo Monacelli

*Dipartimento di Fisica, Università di Roma Sapienza*

(Dated: July 4, 2024)

Understanding and simulating the thermodynamic and dynamical properties of materials affected by strong ionic anharmonicity is a central challenge in material science. Two powerful methodologies have emerged as frontrunners in this exploration: the Self-Consistent Harmonic Approximation (SCHA) with its counterpart, Self-Consistent Phonons (SCP), and the Temperature-Dependent Effective Potential (TDEP). Despite their widespread use, the limitations of these methods are often overlooked, and the absence of a formal derivation for the TDEP has led to significant missteps that hamper its predictive accuracy.

Here, the theoretical foundations of both SCHA and TDEP are revised, unveiling their profound interconnection. This work introduces formal derivation for TDEP, dispelling misconceptions about how to improve its accuracy and refining best practices. The perturbative limit of these methods uncovers that both SCHA and TDEP fall short in reproducing the lowest-order perturbative free energy. While TDEP excels in providing an exact treatment of the static susceptibility, its dynamical extension violates the perturbative regime by overcounting anharmonicity. Conversely, SCHA delivers an approximate static susceptibility but maintains correct static and dynamic response functions within the perturbative limit.

This work introduces a corrective strategy for TDEP's dynamical extension to address these shortcomings. All the claims provided here are benchmarked against the exact (numerical) solution on a simple one-dimensional anharmonic potential.

## I. INTRODUCTION

The development of new methods for electronic structure calculations paved the way to predicting material properties *in silico*. One of the most important advancements concerns determining lattice vibrations from the first principles. Thanks to their energy scale comparable with room temperature, the lattice excitations are responsible for most condensed matter systems' thermodynamics. Therefore, an accurate description of the lattice and its dynamic, the phonons, is pivotal to simulating and predicting the properties of materials. This is challenging in scenarios where the standard Harmonic approximation falls short, like in the proximity of second-order phase transitions.

A particularly relevant case is the study of thermal transport. Here, phonon-phonon scattering is the major limiting factor for heat propagation as temperature increases, with deep technological implications for producing materials with extremely high values of thermal conductivity (heat dissipators) or particularly low ones (insulators). In fact, materials with both low thermal conductivity and electrical resistivity are promising thermoelectrics that can extract energy from heat wasted by other processes. Anharmonic phonon scattering is one of the best strategies to hamper heat diffusion in these good conductors[1].

An exact approach to evaluate thermal transport in materials involves the calculation of the Green-Kubo heat-current autocorrelation function within equilibrium molecular dynamics[2] (MD) or, alternatively, performing non-equilibrium MD simulations with a sustained temperature gradient[3]. However, these methods are ex-

tremely computationally expensive to converge for the system size and simulation time even when fast interatomic force fields are available[4]. Approximate empirical methods based on the Boltzmann transport equation and its quantum counterpart, Wigner transport[5], emerged as the *de facto* state-of-the-art to quantify the thermal conductivity. However, these methods assume a perturbative treatment of phonon-phonon interaction. What happens when they are applied to strongly anharmonic materials, where the harmonic approximation and the quasiparticle picture of phonons breaks down?

The same question arises with other properties depending on lattice motion, like the computation of vibrational spectroscopy within IR and Raman, related respectively to the dipole-dipole and polarizability-polarizability dynamical correlation functions, or the anharmonic phonon dispersion probed by Neutron and inelastic X-ray scattering, related to the dynamical structure factor. In the presence of strong anharmonicity, such as in proximity with second-order displacive phase transitions, the susceptibility diverges, causing a significative deviation of the phonon energies from their harmonic ones, which perturbation theory cannot describe.

Many methodologies have been introduced to address these issues while maintaining the easy phonon quasiparticle description of lattice vibration. Since its first formulation in 1912[6], the Self-Consistent Phonons (SCP) was successfully applied to describe the phonons of noble gasses in their solid phase[7]. Inspired by SCP, many other methods attempted to bridge the concept of phonons to strongly anharmonic materials employing a first-principles approach. The Self-Consistent Ab Initio Lattice Dynamics (SCAILD)[8, 9] was one of the first

methods applied in tandem with *ab initio* simulations. Not too later, many other methodologies emerged[10], some commutated from quantum chemistry to periodic systems, like the vibrational self-consistent field [11]. Among them, the most successful ones in terms of the number of applications and complexity of the materials analyzed are the self-consistent harmonic approximation (SCHA[12–14], with its close relative self-consistent phonons, SCP[15]) and the temperature-dependent effective potential (TDEP[16–18]), which are the focus of this work.

All these methods correct the harmonic phonon dispersion with a nonperturbative self-energy, which can be exploited to compute thermodynamic quantities much more efficiently than standard MD. E.g., thermal conductivity may be obtained by adequately augmenting the Boltzmann-Wigner empirical transport equation[5] with anharmonic spectral functions[19, 20]. A similar approach has been recently applied to unveil the impact of anharmonicity on superconductivity in high-pressure hydrides[21]. However, it has been shown that different theories, and even different implementations among the same theory, lead to distinct phonon dispersions when applied in strongly anharmonic materials[22].

Are the aforementioned methods to simulate phonons in anharmonic systems an uncontrolled form of approximation with questionable predictive power, or is there a way to assess and systematically improve them, determining their accuracy *a priori*?

This work is divided as follows. Sec. II presents the exact definition of phonons in a strongly anharmonic material. Then, Sec. III introduces the equilibrium SCHA and TDEP methods from a rigorous variational principle on the free energy. In particular, TDEP is reformalized, underlying the only implementation based on proper first-principles grounds. Sec. IV discusses the static linear-response theory applied to SCHA and TDEP, unveiling the origin of the observed discrepancies[22], and showing how they can be predicted *a priori* and corrected within both theories. The dynamical response theory is revised in Sec. V, where the TDEP dynamical response function is shown to overcount anharmonicity, violating the perturbative limit. This work introduces a workaround to restore the proper anharmonic limit without extra computational cost. Finally, everything examined in this work is benchmarked against the exact solution of a simple anharmonic potential in Sec. VI. The similarities and differences between SCHA and SCP are discussed in Sec. VII. Sec. VIII presents the perspectives of this work’s findings.

## II. EXACT RESULTS

This work accounts for nuclei as classical particles for simplicity. However, its findings are general and also apply to quantum nuclei.

The exact classical probability distribution in phase

space is defined as

$$\rho_0(\mathbf{p}, \mathbf{r}) = \frac{1}{Z} \exp[-\beta H(\mathbf{p}, \mathbf{r})], \quad (1)$$

where  $\mathbf{r}$  and  $\mathbf{p}$  are the vectors of position and momentum of each particle in the system,  $\beta$  the Boltzmann factor  $\beta = 1/k_b T$ ,  $H(\mathbf{p}, \mathbf{r})$  is the Hamiltonian of nuclei (within the Born-Oppenheimer approximation) and  $Z$  is the partition function defined as a normalization factor for the probability density  $\rho$

$$Z = \int d^{3N} p d^{3N} r \exp[-\beta H(\mathbf{p}, \mathbf{r})]. \quad (2)$$

The knowledge of the partition function allows for computing equilibrium properties of matter through the free energy. At constant temperature, volume, and number of particles (canonical ensemble), the free energy is the one defined by Helmholtz as

$$F(N, V, T) = -\frac{1}{\beta} \ln Z. \quad (3)$$

All thermodynamics observables can be expressed as derivatives of  $F$  to  $N, V, T$ . In particular, the second derivatives of  $F$  are static linear-response quantities discussed in Sec. IV.

The generalized phonons in anharmonic crystals are defined through the lattice’s dynamical response to an external time-dependent perturbation on the nuclei, which coincides with the spectral features extracted from a spectroscopy measurement. The dynamical response is governed by the time propagation of the density distribution by the Liouville equation, acting as a master equation of the system:

$$\frac{\partial \rho}{\partial t} = \sum_{i=1}^{3N} \left( \frac{\partial H}{\partial r_i} \frac{\partial \rho}{\partial p_i} - \frac{\partial H}{\partial p_i} \frac{\partial \rho}{\partial r_i} \right). \quad (4)$$

$\rho(\mathbf{p}, \mathbf{r}, t_0)$  is prepared in equilibrium at time  $t \leq t_0$  where the density distribution satisfies Eq. (1), which is a stationary solution of the master equation (Eq. 4). At  $t = t_0$ , the system interacts with an external perturbation  $H'(t)$ , and the density matrix evolves. In a typical experiment, this perturbation is given by external electric fields (like in the Raman or Infrared), X-rays, or neutron beams. In numerical simulations, perturbing the system with a Dirac delta  $\delta(t - t_0)$  impulse is convenient as it excites all frequencies with the same intensity. This is equivalent to offsetting the equilibrium distribution by a finite momentum along the perturbation direction and studying the free dynamics of the perturbed system. The phonon Green function  $G_{ij}(t)$  is defined as the dynamical response function of the average position of a nucleus when another nucleus is perturbed by a time-dependent external force

$$H'(t) = r_j F(t) \quad (5)$$

$$\langle r_i \rangle(t) = \int_{t_0}^t G_{ij}(t-t')F(t')dt' \quad (6)$$

where

$$\langle r_i \rangle(t) = \int d^{3N}r d^{3N}p r_i \rho(\mathbf{r}, \mathbf{p}, t) \quad (7)$$

and  $F(t)$  is the time profile of the perturbation force on the atom  $j$ . Most of the physical observables can be expressed as functions of the phononic Green's function. Of particular relevance is the so-called spectral function  $\sigma(\omega, \mathbf{q})$ , which refers to the Fourier transform (both in time and space) of the phononic Green function:

$$\tilde{G}_{ij}(\omega, \mathbf{q}) = \frac{1}{N_q} \sum_j e^{i\mathbf{q} \cdot (\mathbf{r}_i - \mathbf{r}_j) - i\omega t} G_{ij}(t), \quad (8)$$

where the sum over  $j$  only runs on the periodic images of the  $i$  with respect to the primitive cell, and  $N_q$  counts the number of supercells included in the summation. The spectral function is the trace of the imaginary part of the Green function

$$\sigma(\omega, \mathbf{q}) = - \sum_{i=1}^{3N_{\text{uc}}} \text{Im} \tilde{G}_{ii}(\omega, \mathbf{q}), \quad (9)$$

where  $N_{\text{uc}}$  counts the number of atoms in the primitive cell. The spectral function  $\sigma(\omega, \mathbf{q})$  presents peaks corresponding with the phonon excitation energies and is proportional to the response function of dynamical experiments, like Raman and IR spectroscopy, X-Ray, and Neutron scattering. The peaks of the spectral function are the real lattice excitations in the presence of anharmonicity and the natural extension of phonons in anharmonic crystals.

### III. THERMODYNAMICS AND PHASE-TRANSITIONS WITHIN SCHA AND TDEP

The exact resummation of the partition function in Eq. (2) quickly becomes intractable for a system containing more than a few degrees of freedom. While there are numerical tools like Monte Carlo and Molecular Dynamics simulations to sample the equilibrium probability distribution  $\rho_0(\mathbf{p}, \mathbf{r})$ , the complete partition function is required to simulate the free energy (Eq. A3). This is where methods like SCHA and TDEP come in handy in providing an approximate definition of the free energy, which can be numerically computed very efficiently even with a system with tens of thousands of atoms. Both methods approach the problem of computing the free energy by introducing a Gaussian trial density matrix defined as

$$\tilde{\rho}(\mathbf{p}, \mathbf{r}) = \frac{e^{-\frac{\beta}{2} \left( \sum_{i=1}^{3N} \frac{p_i^2}{m_i} + \sum_{ij=1}^N \Phi_{ij}(r_i - \mathcal{R}_i)(r_j - \mathcal{R}_j) \right)}}{\mathcal{Z}}, \quad (10)$$

$$\mathcal{Z} = \frac{(2\pi k_B T)^{3N}}{\sqrt{\det \Phi}} \prod_{i=1}^{3N} \sqrt{m_i}. \quad (11)$$

This density matrix is the equilibrium solution of an auxiliary harmonic Hamiltonian

$$\mathcal{H}(\mathbf{p}, \mathbf{r}) = \sum_{i=1}^{3N} \frac{p_i^2}{2m_i} + \frac{1}{2} \sum_{ij} (r_i - \mathcal{R}_i) \Phi_{ij} (r_j - \mathcal{R}_j), \quad (12)$$

$$\mathcal{V}(\mathbf{r}) = \frac{1}{2} \sum_{ij} (r_i - \mathcal{R}_i) \Phi_{ij} (r_j - \mathcal{R}_j). \quad (13)$$

The Gaussian density matrix depends on two tensorial parameters: the average position  $\mathcal{R}$  and the auxiliary force constant matrix  $\Phi$ . Regardless of the trial density matrix, the exact free energy can be evaluated through thermodynamic integration, smoothly changing the probability distribution from the auxiliary Harmonic one into the real one

$$H(\lambda) = \sum_{i=1}^{3N} \frac{p_i^2}{2m_i} + \mathcal{V}(\mathbf{r}) + \lambda [V(\mathbf{r}) - \mathcal{V}(\mathbf{r})]. \quad (14)$$

When  $\lambda = 0$ , we have the auxiliary Harmonic Hamiltonian, with the probability distribution  $\tilde{\rho}(\mathbf{p}, \mathbf{r})$  defined in Eq. (10). When  $\lambda = 1$ , the Hamiltonian becomes the exact one, and the probability distribution is given by Eq. (1). The exact free energy can be evaluated by integrating the free energy derivative with respect to  $\lambda$ :

$$F = F(\lambda = 1) = F(\lambda = 0) + \int_0^1 \frac{\partial F}{\partial \lambda} d\lambda, \quad (15)$$

$$\frac{\partial F}{\partial \lambda} = \left\langle \frac{\partial H}{\partial \lambda} \right\rangle_\lambda = \langle V - \mathcal{V} \rangle_\lambda, \quad (16)$$

Eq. (15) is in principle exact. However, it requires many different simulations to sample the probability distribution  $\rho(\mathbf{p}, \mathbf{r}, \lambda)$ , which is often impractical. SCHA and TDEP offer approximate solutions to the integral in Eq. (15). In particular, it is possible to prove that the integrand  $\langle V - \mathcal{V} \rangle$  is always a strictly decreasing function in  $\lambda$  between 0 and 1. Therefore

$$\langle V - \mathcal{V} \rangle_0 \geq \int_0^1 \langle V - \mathcal{V} \rangle_\lambda d\lambda \geq \langle V - \mathcal{V} \rangle_1. \quad (17)$$

The SCHA and TDEP exploit this property using two different strategies. From Eq. (17) we can derive a variational expression for the upper and lower bound of the free energy

$$F_0 + \langle V - \mathcal{V} \rangle_0 \geq F \geq F_0 + \langle V - \mathcal{V} \rangle_1. \quad (18)$$

The SCHA exploits the left side of the inequality Eq. (18), while TDEP the right side.

$$F \leq F_{\Phi}^{(S)} + \langle V(\mathbf{r}) - \mathcal{V}_{\mathcal{R}, \Phi}^{(S)}(\mathbf{r}) \rangle_{\mathcal{R}, \Phi}^{(S)} \quad (19)$$

$$F \geq F_{\Phi}^{(T)} + \langle V(\mathbf{r}) - \mathcal{V}_{\mathcal{R}, \Phi}^{(T)}(\mathbf{r}) \rangle_{\text{MD}} \quad (20)$$

The difference between the two expressions relies on the ensemble on which the average on the right-hand side is evaluated. For Eq. (19), the ensemble is distributed according to the Gaussian in Eq. (10). The average in Eq. (20), instead, is evaluated when  $\lambda = 1$ , thus on the exact distribution which has to be sampled using molecular dynamics (MD) or Monte Carlo techniques (which is referred to as a  $\langle \cdot \rangle_{\text{MD}}$  in this work). Both inequalities hold for any auxiliary Harmonic Hamiltonian. Therefore, SCHA and TDEP select the dynamical matrix to obtain the best possible free energy estimation. For the SCHA, this corresponds to minimizing the right-hand side of Eq. (19)

$$F_{\text{SCHA}} = \min_{\substack{\mathcal{R}, \Phi \\ \mathcal{R}, \Phi}} F_{\Phi}^{(S)} + \langle V(\mathbf{r}) - \mathcal{V}_{\mathcal{R}, \Phi}^{(S)}(\mathbf{r}) \rangle_{\mathcal{R}, \Phi}^{(S)} \quad (21)$$

The condition that cancel the gradient of  $F(\Phi, \mathcal{R})$  give rise to two self-consistent equations[14]:

$$\Phi_{ab}^{(S)} = \left\langle \frac{\partial^2 V}{\partial r_a \partial r_b} \right\rangle_{\mathcal{R}, \Phi}^{(S)} \quad (22)$$

$$\left\langle \frac{\partial V}{\partial r_a} \right\rangle_{\mathcal{R}, \Phi}^{(S)} = 0. \quad (23)$$

Analogously, the TDEP auxiliary dynamical matrix and centroids maximize the right-hand side of Eq. (20)

$$F_{\text{TDEP}} = \max_{\substack{\mathcal{R}, \Phi \\ \mathcal{R}, \Phi}} F_{\Phi}^{(T)} + \langle V(\mathbf{r}) - \mathcal{V}_{\mathcal{R}, \Phi}^{(T)}(\mathbf{r}) \rangle_{\text{MD}} \quad (24)$$

The zero gradient condition of Eq. (24) provides an equivalent expression for TDEP quantities:

$$\mathcal{R}^{(T)} = \langle \mathbf{r} \rangle_{\text{MD}}, \quad (25)$$

$$\left( \Phi^{(T)-1} \right)_{ab} = \frac{1}{k_b T} \left\langle (r_a - \mathcal{R}_a)(r_b - \mathcal{R}_b) \right\rangle_{\text{MD}} \quad (26)$$

Differently for the self-consistent SCHA equations (Eq. 23 and 22), Eq. (25) and Eq. (26) are one-shot: the right-hand side does not depend on the left-hand side and can be evaluated with one iteration. This comes at the cost of properly sampling the average position and displacement-displacement correlation function exactly within MD or MC. The proof of Eq. 25 and Eq. 26 is reported in Appendix A. The right-hand side of Eq. (26) differs from the procedure reported on the original TDEP works[16, 18, 23]. In fact, the usual TDEP force constants  $\Phi^{(T)}$  are computed by fitting  $\Phi^{(T)}$  on forces from configurations sampled by an MD run. Appendix A 1

demonstrates that Eq. (25) and Eq. (26) also minimize the following least-square cost function:

$$\mathcal{L} = \sum_{a=1}^{3N} \left\langle \left[ f_a(\mathbf{r}) + \sum_b \Phi_{ab}^{(T)} (r_b - \mathcal{R}_b) \right]^2 \right\rangle_{\text{MD}}, \quad (27)$$

$$\frac{\partial \mathcal{L}}{\partial \mathcal{R}^{(T)}} = 0 \quad \frac{\partial \mathcal{L}}{\partial \Phi^{(T)}} = 0 \quad (28)$$

where

$$f_a(\mathbf{r}) = -\frac{\partial V}{\partial r_a}. \quad (29)$$

Therefore, the force constants matrix fitting the first-principle forces  $\mathbf{f}$  sampled by MD or MC also maximizes the TDEP free energy. Interestingly, the order in which the average position  $\mathcal{R}^{(T)}$  and the auxiliary force constant  $\Phi^{(T)}$  are fitted is not important, as the zero-gradient condition of  $\mathcal{R}$  in Eq. (28) does not depend on  $\Phi^{(T)}$ . This equivalence provides formal grounds for the standard TDEP procedure while imposing some constraints. For example, the fit cost function must be a least-square (Eq. 27), and the variational principle remains valid only for a linear fit. Both these choices are fundamental to preserve the variational principle, and their violation leads to wrong results. E.g., fitting higher-order force constants simultaneously with  $\Phi^{(T)}$  in Eq. (27), as suggested in the original TDEP works to improve the accuracy[18], has the opposite detrimental effect of underplaying the role of anharmonicity: an infinite series of high-order force constant matrix recovers the Taylor expansion of the potential where the fitted quantities converge to the trivial terms of the Taylor series. A practical example is reported in Sec. VI, where the fit up to the third order leads to much worse results for free energy and linear response calculations in all tested cases. Fitting higher-order force constants from MD trajectories only makes sense to train cheaper and reliable potentials on which longer simulations can be performed, as implemented in ALAMODE[24]. The other important limitation is the choice of the fitting procedure, which is not arbitrary. For example, if the least-square cost function (Eq. 27) is replaced with any other cost function (like Eq. 3 from the original TDEP paper[16]), the resulting final  $\Phi^{(T)}$  does not maximize the free energy, leading, by definition, to a worse evaluation of the free energy and thermodynamics properties.

Both SCHA and TDEP can be extended to work in the quantum regime. In particular, for the SSCHA, this comes at no extra cost, as the density matrix of a quantum harmonic oscillator remains analytical[14]. In contrast, it presents more difficulties for the TDEP, as molecular dynamics sampling must be replaced by quantum sampling by employing more complex techniques like Path-Integral Molecular Dynamics, which is considerably more expensive.

#### IV. STATIC RESPONSE THEORY

Extending the definition of phonons from the harmonic theory to anharmonic systems at finite temperatures has attracted significant efforts, as it is crucial for addressing changes in phase stability upon heating and cooling. At 0K, neglecting quantum zero-point motion, the (meta)stability of a structure can be evaluated from the absence of imaginary phonons in the harmonic dispersion. In fact, a phonon with an imaginary frequency corresponds to a negative curvature of the total energy along the atomic displacement oriented with the phonon polarization. Since even an infinitesimal displacement in that direction leads to an energy decrease, the structure is in a saddle point of the Born-Oppenheimer energy landscape and is, therefore, unstable. Effects like strain, doping, or temperature can stabilize unstable configurations. However, while it is easy to evaluate changes in the harmonic phonons with the volume, as captured by the quasi-harmonic approximation (QHA), describing changes in the phonon frequencies with the temperature at constant volume is much more challenging.

It is, therefore, tempting to interpret the eigenvalues of the auxiliary dynamical matrix provided by the SCHA and TDEP as temperature-dependent phonons to assess the stability of an atomic structure. This has been done in many works without a proper theoretical justification[13, 15, 20, 22–26]; however, looking for sign changes in eigenvalues of  $\Phi^{(S)}$  and  $\Phi^{(T)}$  is trivially wrong, as it is easy to prove that both  $\Phi^{(S)}$  and  $\Phi^{(T)}$  are positive definite and, when properly converged, never display negative eigenvalues, even when the selected structure is unstable. When evaluating the lowest order perturbative correction of anharmonicity to the harmonic phonons, it was clear that the SSCHA auxiliary force constants  $\Phi^{(S)}$  miss a negative definite term. Therefore, a common *a posteriori* correction employed to the SCHA (and SCP) was to add this extra term empirically, the so-called *bubble* diagram, to the auxiliary phonons, allowing some of the  $\Phi^{(S)}$  eigenvalues to become negative. This term was introduced in the original SCP theory for computing the phonon spectrum of solid Helium and Neon[7, 27], and it has been formalized in the context of the SSCHA by Bianco et al. [28], proving that it emerges naturally from the calculation of the finite temperature free energy Hessian. Due to the positive definite nature of the TDEP force-constant matrix as well (which is evident in Eq. 26), some works attempted to add the bubble diagram also to the phonon dispersion calculated from  $\Phi^{(T)}$ [20]. However, this section shows that TDEP and SSCHA strongly differ in this aspect, as the *bubble* diagram is already accounted for within the TDEP auxiliary matrix, and adding it on top results in overcounting the anharmonicity.

The ionic static response function measures how much the average position of an atom changes when a static

force is applied to it. Applying a static force on atoms results in changing the Hamiltonian into

$$H'(\xi) = H - \sum_{b=1}^{3N} \xi_b (r_b - \mathcal{R}_b^{(T)}) \quad (30)$$

where  $\xi_b$  is the force on the  $b$  atom (including the Cartesian coordinate). The (static) response function  $\chi_{ab}$  is defined as the derivative of the average atomic position with respect to the force applied to the system

$$\chi_{ab} = \frac{\partial \langle r_b \rangle_{\xi}}{\partial \xi_a}. \quad (31)$$

In the TDEP case, whose averages are performed on the exact equilibrium ensemble, the fluctuation-dissipation theorem holds (see Appendix B), leading to

$$\frac{1}{k_b T} \left\langle (r_a - \mathcal{R}_a^{(T)})(r_b - \mathcal{R}_b^{(T)}) \right\rangle_{\text{MD}} = \frac{\partial \langle r_a - \mathcal{R}_a^{(T)} \rangle_{H'(\xi)}}{\partial \xi_b} \Bigg|_{\xi=0}. \quad (32)$$

Thanks to the equivalence in Eq. (26), the ionic static response function is directly related to the TDEP auxiliary force constant matrix

$$\left( \Phi^{(T)-1} \right)_{ab} = \chi_{ab}. \quad (33)$$

Notably, Eq. (33) is exact. Therefore, the TDEP auxiliary phonons can be rigorously interpreted as the exact (dressed up to any order) static response function. The same is not true for the SSCHA. In particular, the average position in Eq. (31) is evaluated on the self-consistent Gaussian distribution, and not on the exact one; therefore, when computing the derivative, an extra term appears due to the explicit dependence of  $\mathcal{R}$  and  $\Phi$  on  $\xi$ . In particular, the SCHA response function is defined by substituting the exact average with the one evaluated on the SCHA Gaussian distribution in Eq. (31)

$$\chi_{ab}^{(S)} = \frac{\partial \langle r_a \rangle_{\mathcal{R}, \Phi, \xi}^{(S)}}{\partial \xi_b} = \frac{\partial \mathcal{R}_a^{(S)}(\xi)}{\partial \xi_b}. \quad (34)$$

To solve Eq. (34), we need to apply perturbation theory to the SCHA equations, similarly to perturbation theory is derived in the framework of other self-consistent theories like Hartree-Fock or DFT. Differentiating the gradients of the SCHA equation with respect to the perturbation  $\xi$ , we get

$$\langle f_a \rangle_{\mathcal{R}(\xi), \Phi(\xi)}^{(S)} = \xi_a, \quad (35)$$

$$\frac{\partial}{\partial \xi_b} \langle f_a \rangle_{\mathcal{R}(\xi), \Phi(\xi)}^{(S)} = \delta_{ab}; \quad (36)$$

$$\Phi_{ab}^{(S)}(\xi) = \left\langle \frac{d^2 V}{dR_a dR_b} \right\rangle_{\mathcal{R}^{(S)}, \Phi^{(S)}(\xi)}, \quad (37)$$

$$\frac{\partial \Phi_{ab}^{(S)}}{\partial \xi_c} = \frac{\partial}{\partial \xi_c} \left\langle \frac{d^2 V}{dR_a dR_b} \right\rangle_{\mathcal{R}, \Phi^{(S)}}. \quad (38)$$

By following all mathematical trivial steps (reported in Appendix C), one arrives at the two coupled linear response equations for the SCHA:

$$\delta_{ab} = - \sum_h \Phi_{ah}^{(S)} \frac{\partial \mathcal{R}_h^{(S)}}{\partial \xi_b} + \sum_{pqlm} \Lambda_{pqlm} \Phi_{pqa}^{(3)} \frac{\partial \Phi_{lm}^{(S)}}{\partial \xi_b}, \quad (39)$$

$$\frac{\partial \Phi_{ab}^{(S)}}{\partial \xi_c} = - \sum_h \Phi_{abh}^{(3)} \frac{\partial \mathcal{R}_h^{(S)}}{\partial \xi_c} - \sum_{pqlm} \Lambda_{pqlm} \Phi_{pqab}^{(4)} \frac{\partial \Phi_{lm}^{(S)}}{\partial \xi_c}, \quad (40)$$

where the  $\Phi^{(3)}$  and  $\Phi^{(4)}$  are the 3 and 4-phonon scattering vertices averaged on the ensemble:

$$\Phi_{abc}^{(3)} = \left\langle \frac{d^3 V}{dR_a dR_b dR_c} \right\rangle_{\mathcal{R}, \Phi^{(S)}}, \quad (41)$$

$$\Phi_{abcd}^{(4)} = \left\langle \frac{d^4 V}{dR_a dR_b dR_c dR_d} \right\rangle_{\mathcal{R}, \Phi^{(S)}}. \quad (42)$$

Inverting simultaneously Eq. (39) and Eq. (40) allows one to compute the SSCHA static response function  $\chi^{(S)}$  of Eq. (34), derived formally for the first time in ref.[28]. The SSCHA expression for the response function is much more complex than the TDEP one. In particular, the auxiliary force constant matrix of the SCHA (Eq. 22) coincides with the inverse of the response function like the TDEP one only in the case  $\Phi^{(3)}$  is exactly zero (and Eq. 39 can be trivially inverted). Notably, no symmetry condition can enforce  $\Phi^{(3)}$  to be zero, as the summation in Eq. (39) runs over the whole Brillouin zone. For example, the inversion symmetry, often wrongly invoked to avoid inverting Eq. (39), cancels out only  $\Phi^{(3)}$  matrix elements at  $\Gamma$  across atoms mapped into themselves by the inversion symmetry. Interestingly, by considering  $\Phi^{(4)} \rightarrow 0$  in Eq. (40), Eq. (39) can be inverted. The extra term correcting  $\Phi^{(S)}$  coincides with the *bubble* diagram derived from perturbation theory[28]. Indeed, Eq. (39) and (40) go beyond perturbation theory as their complete inversion is equivalent to an infinite resummation of RPA-like diagrams, accounting for anharmonicity up to an arbitrary order[28].

The expression for the response function devised here and the SSCHA free energy Hessian derived by Bianco et al.[28] are related as

$$\left( \chi^{(S)} \right)_{ab}^{-1} = \frac{d^2 F_{\text{SCHA}}}{d \mathcal{R}_a d \mathcal{R}_b}, \quad (43)$$

where the dependence of the free energy landscape from the atomic position can be obtained by minimizing  $F_{\text{SCHA}}$  only on the effective force constant matrix, constraining the centroids  $\mathcal{R}^{(S)}$ . The free energy landscape defined in this way coincides with the Landau theory of phase transition: when the curvature of the free energy vanishes with respect to an order parameter  $\Delta$  (function of the atomic positions), the corresponding response function  $\chi$  diverges. This goes beyond the free energy landscape introduced by sampling transition rates in molecular dynamics, as the SCHA does not perform any adiabatic approximation on the order parameter's dynamics.

The response functions of SSCHA and TDEP have a key difference. The SSCHA can study the response function as the inverse of Hessian's atomic free energy landscape, thus defining temperature-dependent static phonons. The solution of the linear-response system (Eq. 39 and 40) may introduce non-positive eigenvalues to the spectrum of the phonons. The crossover between imaginary and real positive phonons is a marker of the critical point in a second-order displacive phase transition. The same is not true within the TDEP. The TDEP dynamical matrix is always positive definite (Eq. (26)), and it coincides with the static response function (Eq. (33)), so there is no extra diagram like the *bubble* one to add that can introduce an imaginary frequency. Indeed, the response function should diverge at the phase transition, thus giving a vanishing frequency in the TDEP dynamical matrix. However, this only occurs in the thermodynamic limit, as in any finite size system Eq. (26) will be finite. This does not change if  $\Phi^{(T)}$  is obtained through the fitting procedure in Eq. (28), as its equivalence with Eq. (26) is always true. Thus, converging to the thermodynamic limit in TDEP (or MD in general) is much trickier than in the SCHA, where a transition point exists even in finite-size systems.

This analysis rationalizes the origin of the discrepancy between SCHA, SCP, and TDEP reported in ref.[22], where the phonon frequencies of SCHA (and SCP) give an apparent worse agreement with the full MD calculations with respect to TDEP ones at low frequencies (thus close to the static limit). Indeed, the TDEP renormalized force constant matrix  $\Phi^{(T)}$  already coincides with the response function, while the SCHA (and SCP) require to invert the Eq. (39) and (40) to obtain the phonons, as  $\Phi^{(S)}$  alone does not carry a valid physical meaning.

A full test of the static susceptibility and the effect of different approximations is reported in Sec. VI B

## V. DYNAMICAL RESPONSE

While static response functions are the key quantities to track second-order phase transitions, as they diverge at the critical point, dynamical response functions probe

the atomic reaction to an external time-dependent stimulus. They are probed by vibrational spectroscopies like Raman, IR, X-rays, and Neutron scattering. Moreover, the dynamical spectral function of phonons encapsulates the phonon lifetimes, and the mean-free-path phonons propagate through the crystal. Thus, it is the fundamental ingredient for calculating the contribution of the lattice to thermal conductivity and plays a major role in simulating electron-phonon properties. The SCHA dynamical response is obtained by performing the analytic continuation at a finite frequency of the static self-energy[7, 27, 28]. This *ansatz* has been proved simultaneously by two independent works to satisfy a variational dynamical principle[29, 30]. Therefore, the SSCHA dynamical response function is formulated on solid first-principles grounds and does not leave room for arbitrary empirical decisions. The analytical continuation at finite frequency is obtained by adding a frequency dependence on the  $\mathbf{\Lambda}$  tensor in Eq. (39) and Eq. (40).

On the contrary, up to very recently, no theoretically grounded approach to obtain dynamical spectral functions was available for TDEP, leading to widespread incorrect practices. The first attempt to formalize a rigorous dynamical expression for the TDEP response function was given by Castellano *et al*[31].

The main challenge of extending TDEP to compute the dynamical response function resides in defining the TDEP self-energy. In fact,  $\overset{(T)}{\Phi}$  is already the exact inverse of the static response function and it does not rely on a many-body definition that can be analytically continued at a finite frequency like the SSCHA or SCP one. A simple analytical continuation of the static response function, like

$$\chi(\omega) = \frac{1}{\omega^2 - \overset{(T)}{\omega}^2}, \quad (44)$$

where  $\overset{(T)}{\omega}$  are the eigenfrequencies of the TDEP dynamical matrix

$$\sum_b \frac{\overset{(T)}{\Phi}_{ab} e_\mu^b}{\sqrt{m_a m_b}} = \overset{(T)}{\omega}_\mu^2 e_\mu^a, \quad (45)$$

unavoidably leads to a vanishing imaginary part and a non-dissipative system, which prevents accessing crucial information like the phonon lifetime. This problem can be manually “fixed” by computing the lifetime of phonons exploiting the Fermi golden rule by fitting the third-order force constant matrix together with  $\overset{(T)}{\Phi}$  in Eq. (27)[23]. However, we already proved in Sec. III that this fit violates the variational principle and must be avoided. An alternative strategy is to fit a third-order force constant on the residual forces, keeping  $\overset{(T)}{\Phi}$  fixed, similar to how high-order force constants are defined within the SSCHA. This approach is justified by the mode-coupling theory[31], leading to much better results.

Then, to achieve a nonperturbative response similar to the one obtained from the SSCHA, the Kramers-Kronig relations can be employed to correct the dynamical frequencies of phonons self-consistently[31]. However, extra care must be taken at this stage: the real part of the *bubble* self-energy does not vanish for  $\omega \rightarrow 0$ , thus violating the exact result achieved by TDEP in the static case (and the perturbative limit). A similar result affects the frequency shift computed from Kramers-Kronig relations, as the  $\lim_{\omega \rightarrow 0} \omega \Delta(\omega) \neq 0$  in Eq. (53) and (56) of ref.[31] for  $\mu = \nu$ , where  $\omega \Delta(\omega)$  quantifies the frequency shift introduced by the anharmonic phonon scattering. This contradiction arises from an intrinsic ambiguity of Kramers-Kronig relations, which defines the real part of an analytic function up to a constant. To avoid the ambiguity of Kramers-Kronig relations, they can be replaced with the complex self-energy arising from the *bubble* diagram, where

$$(\chi^{-1})_{ab}(\omega) = \delta_{ab} \omega^2 - \frac{\overset{(T)}{\Phi}_{ab} + \Pi_{ab}(\omega)}{\sqrt{m_a m_b}} \quad (46)$$

$$\Pi_{ab}(\omega) = \sum_{pqrs} \overset{(3)}{\Phi}_{apq} \Lambda(\omega)_{pqrs} \overset{(3)}{\Phi}_{rsb} \quad (47)$$

and  $\Lambda_{pqrs}(\omega)$  is the opposite of twice the two-phonons propagator[28]. The self-energy  $\Pi_{ab}(\omega)$  is complex and arises from a phonon that scatters (or decays) with other phonons through the 3-body interaction term  $\overset{(3)}{\Phi}$ . The imaginary part of Eq. (47) coincides with the Fermi golden rule applied to the three-phonons scattering processes. This self-energy overlaps with the SSCHA one when  $\overset{(4)}{\Phi} \rightarrow 0$  in Eq. (40). Also here, the  $\omega \rightarrow 0$  of Eq. (46) does not become the exact static TDEP susceptibility (Eq. 33), as  $\overset{(T)}{\Phi}$  already accounts for the real-part of the *bubble* correction (and beyond); therefore, dressing TDEP phonons with the *bubble* self-energy leads to overcounting anharmonicity and violating the perturbative regime.

Luckily, this problem has a straightforward solution: removing the static limit of the *bubble* self-energy from the calculation of the dynamical response function:

$$(\chi^{-1})_{ab}(\omega) = \delta_{ab} \omega^2 - \frac{\overset{(T)}{\Phi}_{ab} + \Pi_{ab}(\omega) - \Pi_{ab}(\omega \rightarrow 0)}{\sqrt{m_a m_b}}. \quad (48)$$

Eq. (48) reproduces the correct  $\omega \rightarrow 0$  limit and also satisfies the lowest-order perturbation theory at finite  $\omega$ . Eq. (48) also generates the correct second-order memory kernel for the mode-coupling theory derived in ref.[31] while fixing the ambiguities of the Kramers-Kronig transformations.

Differently from the SSCHA, where the full dynamical response is obtained from an infinite resummation of diagrams emerging from the inversion of Eq. (39) and (40),

the correction in Eq. (48) is defined perturbatively adding more scattering processes in the self-energy (or the memory kernel in the language of mode-coupling theory[31]). However, perturbative truncations of the self-energy result in the violation of the response functions' sum rules. Only the complete inversion of the SSCHA equations (Eq. 39 and 40) leads to a response function that satisfies all the correct sum rules[7, 27, 32], while truncating the inversion to the *bubble* diagram does not. For this reason, there is no complete dynamical expression for the TDEP response function that correctly satisfies all sum rules. This is crucial when computing properties for  $q \rightarrow 0$ , such as the bending rigidity of 2D materials[32], which may diverge if the self-energy is truncated at any finite order.

A numerical test for the perturbative regime of TDEP and SSCHA dynamical spectral functions is reported in Sec. VIC.

## VI. NUMERICAL COMPARISON

This section tests the SSCHA and TDEP thermodynamics (free energy), static response, and dynamical response functions against an exact (numerical) benchmark.

Let us consider a particle in a 1D anharmonic potential of the form

$$V(x) = \frac{1}{2}ax^2 + \frac{1}{6}bx^3 + \frac{1}{24}cx^4. \quad (49)$$

The anharmonicity of this simple potential can be gradually switched on by tuning the  $b$  and  $c$  parameters. To isolate the role played by the third order anharmonicity (the  $b$  parameter), we set  $a = 1.0 E_h/a_0^2$  and  $c = 1.0 \times 10^{-4} E_h/a_0^4$ , just big enough to avoid run-away solutions while tuning  $b$ .

Although this may seem trivial, a systematic benchmark comparing TDEP and SSCHA was still missing.

### A. Free energy

All thermodynamic quantities can be inferred from derivatives of the free energy. In this section, the free energy obtained within SSCHA (Eq. 21) and TDEP (Eq. 24) is benchmarked. To provide a comprehensive comparison, also the pure vibrational contribution to the TDEP free energy is evaluated, as performed by some TDEP implementations[33].

The simulations are conducted for  $\beta = 1 E_h$  ( $E_h$  is Hartree atomic units) by varying the third-order anharmonicity  $b$ , and reported in FIG. 1. Both the SSCHA and TDEP (only when fitted up to second-order) offer variational expressions to the free energy following the inequalities presented in Sec. III (Eq. 21 and 24). The TDEP fit with the third-order force constants leads to much worse results, recovering the correct answer only in

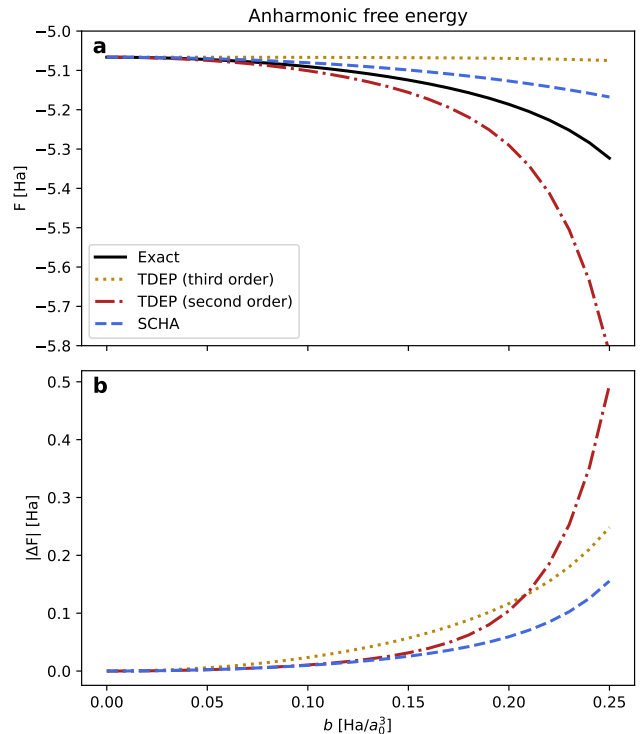


FIG. 1. Free energy (a) of the potential Eq. (49),  $\beta = 1 E_h$ , comparing the exact (numerical) solution with SSCHA and TDEP. Panel (b) reports the absolute value of the error versus the exact solution. The TDEP is implemented in two flavors: i) by fitting only the second-order force constant and then computing the free energy as in Eq. (24), ii) by fitting up to the third-order force constant matrix and removing the high-order terms of the expansion to reduce the fluctuations, as reported in Eq. (50) and (51) (also 24-25 of ref.[33]).

the harmonic potential ( $b \rightarrow 0$ ). This may be surprising since the potential of Eq. (49) is cubic, and the fit up to third-order force constants is exact. However, by inspecting the expression implemented in TDEP packages[33] for the free energy, the reason appears evident:

$$V^{(n)} = \left\langle V(\mathbf{r}) - \sum_{p=1}^n \frac{1}{p!} \sum_{a_1 \dots a_p} \Phi_{a_1 \dots a_p}^{(p)} \prod_{k=1}^p (R_{a_k} - \langle R_{a_k} \rangle^{(T)}) \right\rangle, \quad (50)$$

$$F_{\text{TDEP}}^{(n)} = V^{(n)} + \frac{3}{2} N k_B T - T S[\Phi^{(T)}]. \quad (51)$$

Eq. (51) does not tend to the exact free energy for  $n \rightarrow \infty$  (it is not the cumulant expansion of the free energy). Therefore, there is no reason why increasing  $n$  would improve the result's quality. Quite the opposite: in the  $n \rightarrow \infty$  limit, TDEP fits the potential with the temperature-independent Taylor expansion. Then, Eq. (50) coincides with the value of the potential energy in the average position

$$\lim_{n \rightarrow \infty} V^{(n)} = V(\langle \mathbf{R} \rangle^{(T)}),$$



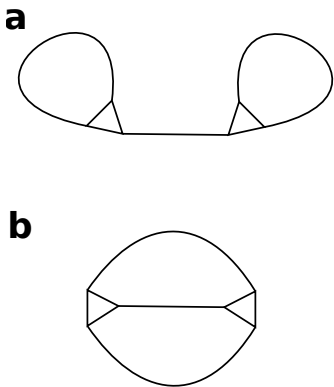


FIG. 2. The two lowest-order Feynman diagrams for the free energy correction in the cubic anharmonicity. The triangles represent the three-phonon scattering vertex  $\Phi^{(3)}$ , while lines the one-phonon propagator. While **a** is accounted for within the SSCHA, the **b** is not. The derivation and expression of these diagrams are reported in Appendix D.

and the second-order fitted force constant  $\Phi^{(T)}$  coincides with the harmonic perturbative term of the Taylor expansion. Therefore, Eq. (51) becomes the free energy within the Harmonic approximation. For the potential in Eq. (49), since  $c$  is small, already a third-order fit is enough to recover the almost perfect harmonic limit, and the free energy obtained by this approach does not depend on the degree of anharmonicity  $b$ . The main reason for this failure relies on the fact that the high-order terms fitted from the potential should be included in the expression for the entropy  $S$  in Eq. (51), however, this is not feasible, as entropy has an analytical expression only for quadratic potentials.

This is the first demonstration that the TDEP method leads to good results only if the fit is limited to second-order force constants, as anticipated in Sec. III. Notably, even if both the second-order TDEP and the SSCHA satisfy a variational condition on the free energy, the SSCHA performs better for stronger anharmonicity.

FIG. 1 shows how both TDEP and SSCHA violate the perturbative limit of the free energy for  $b \rightarrow 0$ . In fact, the lowest-order correction to the free energy is quadratic in the third order anharmonicity  $b$  and can be recast in the two Feynman diagrams reported in FIG. 2 (derived in Appendix D)

As was discussed by ref.[34], the SSCHA is limited to all possible Feynman diagrams in which each cut at time  $t$  can intersect at most 2 phonon lines. In other words, the SSCHA cannot describe more than 2 photons propagating simultaneously throughout the system. While the one-phonon Green function does not have any of such diagrams at the lowest order of perturbation theory, making the response function correct in the perturbative limit, the same is not true for the free energy, where at the lowest order a diagram containing three simultaneous phonon lines contributes (FIG. 2**b**). This translates into a wrong curvature (second derivative for  $b \rightarrow 0$ ) for

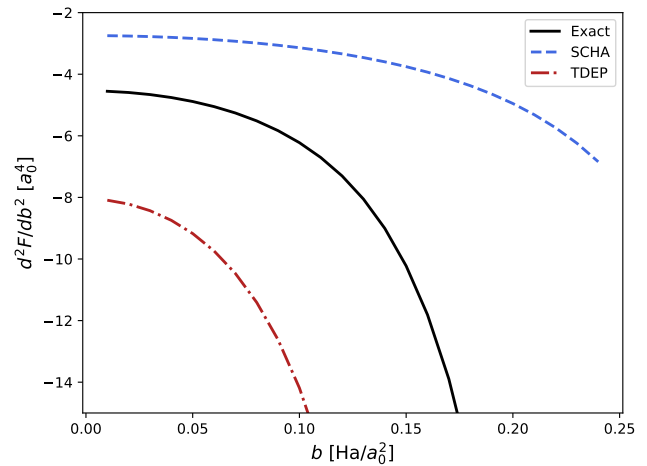


FIG. 3. Curvature of the free energy with respect to the third order coefficient  $b$ . SCHA and TDEP fail to reproduce the correct free energy curvature on the anharmonicity in the  $b \rightarrow 0$  limit.

the free energy as a function of anharmonic parameter  $b$ . Indeed, the TDEP free energy also predicts the wrong curvature of the free energy, thus accounting for the two diagrams of FIG. 2 with wrong prefactors. The error on the curvature of both SCHA and TDEP, as shown FIG. 3, has an opposite sign for  $b \rightarrow 0$ , but it is not the same. For this reason, computing the Free energy as the average between SCHA and TDEP, while in some cases it may improve the absolute value of the free energy, still fails in reproducing the perturbative limit and also comes at the cost of violating the variational expression, which is particularly useful in computing the phase diagram by assuring a (partial) error cancellation when comparing free energies of different phases.

## B. The static linear response theory - second-order phase transitions

This section compares the SCHA and various TDEP flavors to describe the static response function. Static response functions are fundamental to predict second-order phase transitions as the susceptibility diverges at the critical point. The static susceptibility of the model in Eq. (49) is computed as described in Sec. IV: it is the derivative of the average atomic position upon the application of an external uniform force  $\xi$  (Eq. 31). The exact result has been evaluated numerically by computing the algorithmic differentiation of the average position  $\langle R \rangle_\xi$  by integrating with the trapezoid method over the distribution:

$$p(R, \xi) = \frac{e^{-\beta[V(R) - \xi R]}}{\int_{-L}^L e^{-\beta[V(R) - \xi R]}} \quad (52)$$

where  $L$  is set to  $10 a_0$  to converge the result.

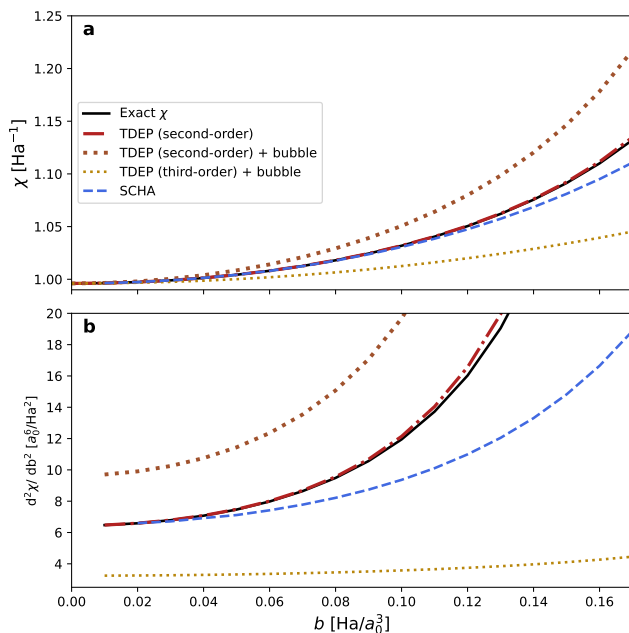


FIG. 4. Comparison of the static response function between TDEP, SCHA and the exact result. Panel **a** reports the susceptibility  $\chi$  as a function of the anharmonicity. Panel **b** shows the second derivative of  $\chi$  for the third-order anharmonic parameter  $b$ . Only SCHA and TDEP (second-order) present the correct  $b \rightarrow 0$  limit, demonstrating how they are the only two approaches that correctly reproduce the perturbative result.

FIG. 4 compares the static susceptibility from SCHA and two TDEP flavors with the exact result. As discussed in Sec. IV, the standard TDEP dynamical matrix  $\Phi^{(T)}$  (without any correction) matches the exact result independently on the degree of anharmonicity. This is a consequence of the fluctuation-dissipation theorem, as  $\Phi^{(T)}$  coincides with the inverse of the covariance matrix. FIG. 4b shows the perturbative limit of the response function. The SCHA and the (second-order) TDEP static susceptibilities have the correct curvature versus the  $b$  parameter (perturbative limit). This was already demonstrated for the SSCHA in ref.[28] and, up to my knowledge, never proved for TDEP.

The same FIG. 4b also shows how two other commonly employed approaches for TDEP fail. As discussed in Sec. IV, TDEP force constant matrix  $\Phi^{(T)}$  is always positive definite, as it is equal to the position-position static correlator, even if the centroid positions are constrained to an unstable position. Therefore, exploiting  $\Phi^{(T)}$  to assess a structure's stability is impossible. For this reason, a bubble diagram contribution is sometimes added to  $\Phi^{(T)}$  (FIG. 5b) in the hope of describing a transition to a saddle point of the free energy landscape to disentangle the stability of a structure. For example, in ref.[20] the

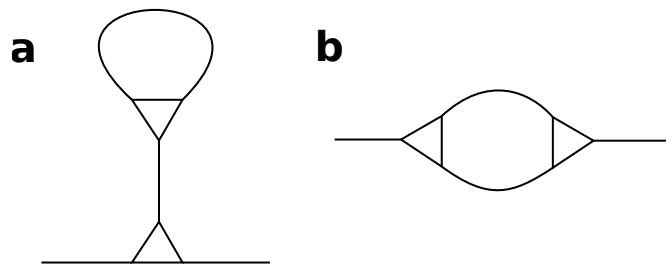


FIG. 5. Lowest order diagrammatic correction to the static response function. The triangle represents the three-phonon scattering vertex  $\Phi^{(3)}$ , while a solid line is the phonon propagator. Panel **a** reports the *tadpole* diagram, responsible for the change of the centroids  $\langle r \rangle$  due to anharmonicity (real self-energy). Panel **b** displays the *bubble* diagram, whose dynamical equation is reported in Eq. 47. Both diagrams are quadratic in  $\Phi^{(3)}$ , and the lowest order correction of anharmonicity to the static and dynamic susceptibilities.

TDEP  $\Phi^{(T)}$  is corrected with the static self-energy of the *bubble* diagram  $\Pi(\omega \rightarrow 0)$  (Eq. D10) to assess the phase transition between rhombohedral and cubic GeTe. However, this procedure leads to wrong results as proved in Sec. IV: adding the extra bubble diagram leads to overcounting anharmonicity. The absence of a divergence in the bare TDEP susceptibility  $\Phi^{(T)}$  observed in ref.[20] is either a sign of a nondisplacive phase-transition in GeTe or a manifestation of the difficulties in converging TDEP results in the proximity of a phase-transition, with the latter being more likely as confirmed by a subsequent analysis from some of the same authors only relying on more expensive but exact MD correlation functions[35].

As we discussed for the free energy, fitting higher-order force-constant matrices (above second order) to minimize the least square error of forces leads to wrong results. In this case, the anharmonicity is undersampled, as the resulting second-order force constant matrix matches with the harmonic force-constant matrix (due to the negligible value of  $c$  in Eq. 49). The only correction to evaluate the susceptibilities from the harmonic susceptibilities by TDEP comes from the *bubble* diagram (FIG. 5b), thus missing the role played by the *tadpole* (FIG. 5a) and underestimating the perturbative limit (FIG. 4b).

### C. Dynamical spectral functions

One of the most promising applications of SSCHA and TDEP is the calculation of dynamical spectral functions, which play a dominant role in estimating the lattice thermal conductivity.

The exact dynamic response function is evaluated by numerically solving the Liouville equation (Eq. 4). The equilibrium solution is perturbed with a time-dependent potential  $V'(x, t) = x\delta(t - t_0)\Delta$ , where  $\delta(t - t_0)$  is the Dirac's delta function, here employed to excite all fre-

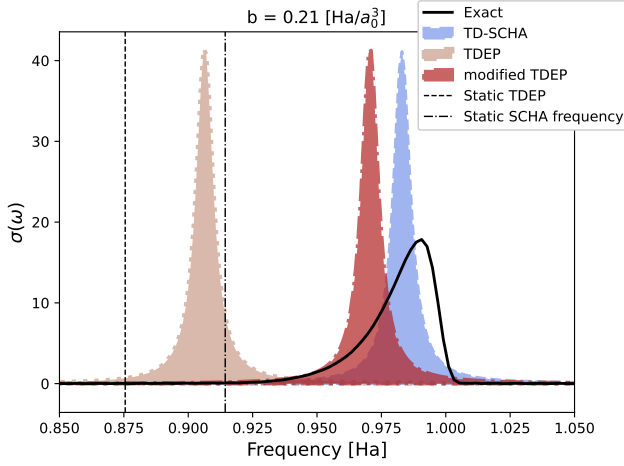


FIG. 6. Dynamical spectral function of the 1D potential Eq. (49) where  $b = 0.21 E_h/a_0^3$  and  $k_B T = 1 E_h$ . All the spectral functions with TDEP and TD-SCHA have an imaginary smearing of  $\eta = 4 \times 10^{-3} E_h$ . The vertical dashed (dash-dot) lines represent the pole of the static TDEP (SCHA) response function.

quencies with the same amplitude. This results in a shift of the momentum  $p$  of the equilibrium distribution by a (small) finite value  $\Delta$

$$\rho(x, p, t_0^+) = \rho(x, p + \Delta, t_0^-) \quad (53)$$

$$\rho(x, p, t_0^+) = \frac{\exp\left[-\beta\frac{(p+\Delta)^2}{2m} - \beta V(x)\right]}{Z}. \quad (54)$$

Then, the response function is evaluated as the Fourier transform of the average position as a function of time (Eq. 7 and 8). The Liuville equation is solved with finite differences on a grid between  $-4 a_0$  and  $4 a_0$  discretized by  $\Delta x = 0.05 a_0$ ,  $\Delta p = 0.05 a_0^{-1}$ , and  $\Delta t = 2.5 \times 10^{-3} E_h^{-1}$ , with a perturbation  $\Delta = 0.1 a_0^{-1}$

FIG. 6 reports the comparison between the exact spectral function and the one obtained by TDEP, TD-SCHA, and the modified TDEP proposed by this work for  $b = 0.21 E_h/a_0^3$ . The TDEP spectral function is evaluated by adding to the static response the dynamic self-energy contribution of the bubble diagram (FIG. 5b). The modified TDEP spectral function differs from the standard TDEP as the static ( $\omega \rightarrow 0$ ) limit of the same bubble diagram is removed from the total self-energy, as explained in Sec. V, Eq. (48).

As can be seen, the real part of the *bubble* self-energy, emerging by Kramers-Kronig relationships, produces a global red-shift of the frequencies, leading to a worse agreement than TD-SCHA with the exact result. Another interesting feature depicted in FIG. 6 is the distance between the TD-SCHA and the TDEP spectral function peak and their respective static susceptibility pole. This difference originates from the real part of the

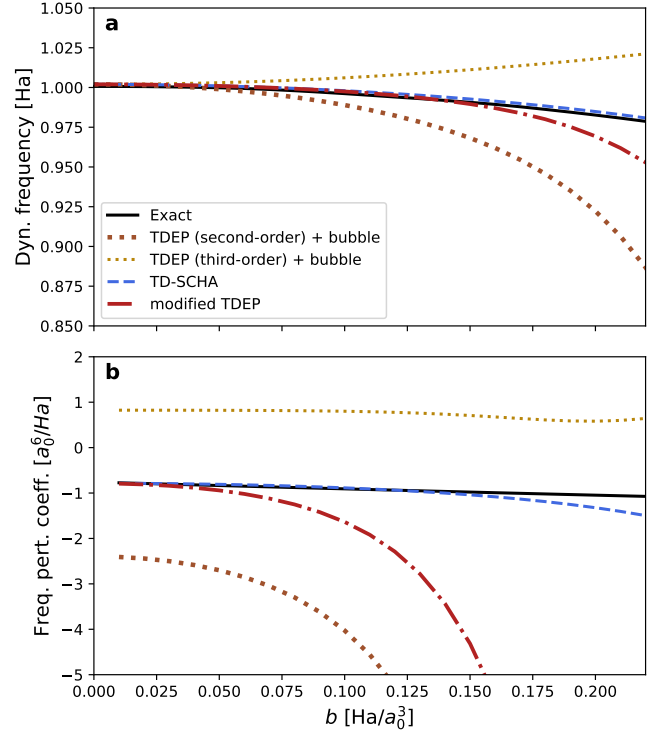


FIG. 7. Dynamical frequency computed as the pole of the spectral function  $\sigma(\omega)$  (FIG. 6) comparing different approximations (potential reported in Eq. 49) Panel **a**: Poles of the spectral functions. Panel **b**: second-derivative of the poles as a function of the anharmonicity  $b$ . Lines matching the poles for  $b \rightarrow 0$  indicate a correct perturbative limit.

bubble diagram self-energy that depends on frequency, and it is smaller at finite frequencies rather than at  $\omega \rightarrow 0$ .

To further investigate the discrepancies with the exact results of the various approximations, FIG. 7a compares the average position of the spectral peak (the pole of the spectral function) as a function of the third order anharmonicity (the  $b$  parameter). As always, all the methods give the exact result in the harmonic limit ( $b \rightarrow 0$ ). However, as we introduce anharmonicity, only the TD-SCHA and the modified TDEP provide the correct perturbative coefficient. This is well shown by FIG. 7b, where the second derivative of the dynamical average frequency with  $b$  is reported. The standard TDEP approach violates the perturbative limit by double counting the bubble diagram in FIG. 5b, which is already accounted for at the static level. The agreement of TDEP is, in fact, much improved if the static limit ( $\omega \rightarrow 0$ ) of the bubble diagram is removed from the real part of the self-energy and then added back with the full frequency dependence, as done in the modified TDEP (Eq. 48). Pure TDEP dressed with the bubble diagram violates the perturbative regime. Notably, the TDEP computed using the full fit of the potential energy landscape up to the third order performs even worse than the harmonic approxi-

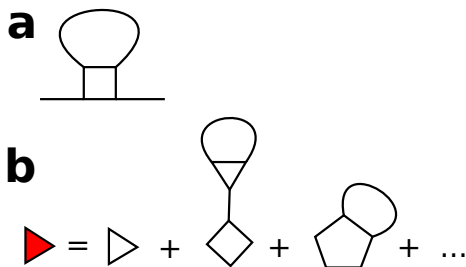


FIG. 8. Anharmonic diagrams that can be accounted for in the SCP theory. Panel **a** reports the *loop* diagram: the lowest order correction of the four-phonon scattering vertex  $\Phi^{(4)}$ . Panel **b** shows how phonon-phonon scattering vertices can be re-normalized, accounting for higher-order terms. Tadpole-like corrections appended to one vertex account for the change of average position due to third-order anharmonicity, while a loop connecting two vertices accounts for the effect that higher-order terms of the phonon-phonon interaction have when taking the average (Eq. 41 and 42)

mation. Despite this important discrepancy in the position of the dynamical vibrational frequency, all of these methods still give the correct perturbative value for the imaginary part of the self-energy, thus predicting reasonable values for the phonon lifetimes. In fact, phonon lifetimes depend on the imaginary part of the bubble diagram, which is nonzero only at finite frequency. This means that all the approaches discussed so far correctly evaluate the imaginary part of the self-energy in the perturbative scheme, as it is equivalent to the Fermi Golden rule.

This is probably the reason for the success of all different implementations of TDEP in computing thermal transport properties, where most of the contribution is given by the phonon lifetimes related to the imaginary part of the self-energy. However, in strongly anharmonic systems outside the perturbative regime, these differences in the phonon frequencies arising from the real part of the self-energy may hamper the accurate estimation of thermal transport properties, and the correction proposed in Eq. (48) becomes essential.

## VII. SELF-CONSISTENT PHONONS

The Self-Consistent Phonons (SCP) approach originates from the many-body theory and has a very long history[6]; it is the phononic equivalent of Hartree-Fock for electrons. It solves the Dyson equation for the phonons' Green function self-consistently by truncating the self-energy to a given order. The method comes in multiple flavors depending on the processes accounted for in the self-energy.

The simplest and most common implementation of SCP is truncating the self-energy only to the *loop* diagram (FIG. 8a).

The self-consistency originates from the propagator

that loops on the four-phonon scattering matrix  $\Phi^{(4)}$ , which depends on the  $t \rightarrow 0^+$  phonons' Green function:

$$\Phi_{ab}^{(\text{SCP})} = \Phi_{ab}^{(0)} + \Pi_{ab}(\Phi^{(\text{SCP})}) \quad (55)$$

$$\Pi_{ab}(\Phi^{(\text{SCP})}) = \frac{1}{2} \sum_{cd} \Phi_{abcd}^{(4)} \langle (R_c - \mathcal{R}_c)(R_d - \mathcal{R}_d) \rangle_{\Phi^{(\text{SCP})}}. \quad (56)$$

SCP was successfully applied in solid helium[7], where, due to the high symmetry of the structure, only the frequencies of the  $\Phi^{(\text{SCP})}$  must be updated in the self-consistent cycle. Interestingly, this approach reduces itself to the SCHA in a crystal where all the lattice positions are constrained by symmetry (eliminating the *tadpole* diagram in FIG. 5a), and if the interatomic potential is at most quartic. However, even in this limit, the phonons determined by SCP considering only the loop still violate the perturbative limit as no symmetry argument can cancel out the bubble diagram (FIG. 5b). For similarity with perturbation theory, the bubble diagram is often added *a posteriori* after the self-consistency of the loop is achieved. This has been employed for the first time to study the phonon spectra of solid neon[36], and more recently employed, e.g., in the simulation of SrTiO<sub>3</sub> cubic phase[15], where all the parameters of the lattice are constrained by the  $Pm\bar{3}m$  symmetry group, thus leading to a result that correctly reproduces the perturbative limit both in  $\Phi^{(4)}$  and in  $\Phi^{(3)}$ . Indeed, the SCP method can be easily improved to add the contribution of diagram FIG. 2b also *a posteriori* for the calculation of the free energy[37], and to relax the hypothesis of crystal lattice position fully constrained by symmetry[38] by adding the *tadpole* in the expression of the self-consistent self-energy (FIG. 5a) and by renormalizing the anharmonic scattering vertices based on the relaxed structure (FIG. 8b) by dressing high-order scattering vertices with tadpole diagrams.

Given its diagrammatic origin, this method is built on a rigorous perturbative expansion of the solution with anharmonicity. Therefore, it leads to a result that matches perturbation theory up to any arbitrary order, thus beating the limits of TDEP and SCHA encountered in this work. The other side of the medal is that correcting high-order terms comes at an exponentially high computational cost, thus limiting its practical applicability only to describe the first-order corrections.

An intrinsic limitation of the SCP method is that it remains bound to the Taylor expansion of the interatomic potential, which becomes significantly more expensive as the order increases. Moreover, the SCP Green's function and susceptibilities do not emerge from a variational approach (except when the self-energy is truncated to reproduce the SSCHA, for which the two methods coincide). This has two consequences that must be considered carefully when employing this methodology: i) nonvariational free energy does not necessarily lead to error cancellation across different phases, and increasing the self-energy's

order does not necessarily convert into a more accurate phase diagram. ii) a nonvariational self-energy leads to sum rule violations. An example of the sum rule violation of the first-order SCP theory occurs in freestanding 2D materials, where the truncation of the self-energy leads to a linear dispersion of the flexural mode around the center of the Brillouin zone. In contrast, by symmetry arguments, the exact solution must exhibit a quadratic dispersion[32].

## VIII. CONCLUSIONS

This work systematically compared different methodologies to simulate strongly anharmonic crystals. The first-principle grounds for the TDEP introduced here shed new light on the different TDEP implementations, providing a unique receipt to perform accurate simulations. To summarize them: i) never fit beyond the second-order force constant. ii) employ a progressive fit over residual forces to extract higher-order contributions. iii) Always use a least-square cost function for fitting. iv) Do not correct the static-response function. v) Any process considered for evaluating phonon lifetimes should also be removed in the limit  $\omega \rightarrow 0$  from the real part of the self-energy (as reported in Eq. 48).

We unveiled how SSCHA and TDEP share a common origin as variational principles on the free energy and explained the origin of the observed discrepancies[22]. Both of them fail to reproduce the perturbative limit of the free energy. While it is possible to correct the SSCHA and SCP a posteriori[37], this violates the variational principle, which may compromise the accuracy of a phase diagram estimation.

Despite the failure of available TDEP implementations in reproducing the perturbative limit of the phonon energies, reasonable results can still be obtained for the thermal transport properties, as the dominant contribution arises from the phonon lifetimes, correct in the perturbative limit regardless of the kind of TDEP implementation adopted. Indeed, this study reveals how much more care must be taken for strongly anharmonic crystals, where the real part of the phonon-phonon self-energy may play a crucial role, as it occurs when predicting the outcome of spectroscopy measurements, where the TD-SCHA is still the most reliable approximate method available[39–41], especially for correcting anharmonicity beyond the second-order while satisfying all sum rules of the crystal[32].

## ACKNOWLEDGMENTS

I acknowledge Giovanni Caldarelli, Antonio Siciliano, and Francesco Mauri for our helpful discussions.

## Appendix A: Proof of the TDEP method

While introduced long ago, a rigorous formal derivation of the TDEP method is still difficult to find in the literature, as it is typically presented as a generic fit of the potential energy landscape on a finite temperature MD run. Consequently, the TDEP method comes with many flavors, such as the order of the temperature-dependent force constants and the cost function employed in the fit, usually chosen empirically. For this reason, here we derive the TDEP method from the variational principle of the free energy presented in the main text, namely Eq. (24), which defines a unique and precise strategy in which the fit on the MD trajectory must be performed.

The  $\mathcal{R}^{(T)}$  and  $\Phi^{(T)}$  parameters maximizing the free energy satisfy Eq. (24). For the centroids  $\mathcal{R}$ , the only term in the TDEP free energy depending on it is the auxiliary potential  $\mathcal{V}_{\mathcal{R}, \Phi}^{(T)}(\mathbf{r})$ , from which we get the condition

$$\frac{\partial}{\partial \mathcal{R}_a} \sum_{ij} \left\langle (r_i - \mathcal{R}_i) \Phi_{ij}^{(T)} (r_j - \mathcal{R}_j) \right\rangle_{\text{MD}} = 0, \quad (\text{A1})$$

which trivially leads to

$$\mathcal{R}_a = \langle r_a \rangle_{\text{MD}}, \quad (\text{A2})$$

corresponding to Eq. (25). A bit more complex is the equation for  $\Phi$ , as both  $\mathcal{V}_{\mathcal{R}, \Phi}^{(T)}(\mathbf{r})$  and the harmonic free energy  $F_{\Phi}^{(T)}$  depend on it. Let us start with the derivative of the auxiliary harmonic free energy, which can be computed from the partition function as

$$F_{\Phi}^{(T)} = -\frac{1}{\beta} \ln Z_{\Phi}^{(T)}. \quad (\text{A3})$$

By replacing Eq. (2) into Eq. (A3), we get

$$F_{\Phi}^{(T)} = k_B T \left[ \frac{1}{2} \ln \left( \det \Phi^{(T)} \right) - \sum_{i=1}^{3N} \ln (2\pi k_B T \sqrt{m_i}) \right]. \quad (\text{A4})$$

Thus, the derivative of the free energy on  $\Phi$  only depends on the first term

$$\frac{\partial F_{\Phi}^{(T)}}{\partial \Phi_{ab}^{(T)}} = \frac{k_B T}{2} \frac{\partial}{\partial \Phi_{ab}^{(T)}} \ln \left( \det \Phi^{(T)} \right) \quad (\text{A5})$$

We can now exploit the definition of the determinant. Let  $\lambda_k$  be the  $k$ -th eigenvalue of the  $\Phi^{(T)}$  symmetric matrix, and  $e_k^i$  be the  $i$ -th component of the corresponding  $k$ -th eigenvector, the determinant is the product of the

eigenvalues

$$\begin{aligned} \frac{\partial}{\partial \Phi_{ab}^{(T)}} \ln \left( \det \Phi^{(T)} \right) &= \frac{\partial}{\partial \Phi_{ab}^{(T)}} \ln \left( \prod_{k=1}^{3N} \lambda_k \right) \\ &= \frac{\partial}{\partial \Phi_{ab}^{(T)}} \sum_{k=1}^{3N} \ln \lambda_k \\ &= \sum_{k=1}^{3N} \frac{1}{\lambda_k} \frac{\partial \lambda_k}{\partial \Phi_{ab}^{(T)}} \end{aligned} \quad (\text{A6})$$

The derivative of the  $k$ -th eigenvalue on the Matrix element  $\Phi_{ab}^{(T)}$  can be evaluated within perturbation theory

$$\frac{\partial \lambda_k}{\partial \Phi_{ab}^{(T)}} = e_k^a e_k^b, \quad (\text{A7})$$

$$\frac{\partial}{\partial \Phi_{ab}^{(T)}} \ln \left( \det \Phi^{(T)} \right) = \sum_{k=1}^{3N} \frac{e_k^a e_k^b}{\lambda_k}. \quad (\text{A8})$$

The right-hand side of Eq. (A8) is the inverse of the  $\Phi^{(T)}$  matrix decomposed on the basis that diagonalizes  $\Phi^{(T)}$ .

$$\frac{\partial}{\partial \Phi_{ab}^{(T)}} \ln \left( \det \Phi^{(T)} \right) = \left( \Phi^{(T)-1} \right)_{ab} \quad (\text{A9})$$

Thus, we get

$$\frac{\partial F_{\Phi}^{(T)}}{\partial \Phi_{ab}^{(T)}} = \frac{k_B T}{2} \left( \Phi^{(T)-1} \right)_{ab} \quad (\text{A10})$$

The other part of the gradient comes from the average of the auxiliary Harmonic potential

$$\frac{\partial F_{\Phi}^{(T)}}{\partial \Phi_{ab}^{(T)}} - \frac{\partial \langle \mathcal{V}_{\mathcal{R}, \Phi}^{(T)} \rangle_{\text{MD}}}{\partial \Phi_{ab}^{(T)}} = 0 \quad (\text{A11})$$

From this we get

$$\frac{k_B T}{2} \left( \Phi^{(T)-1} \right)_{ab} - \frac{1}{2} \left\langle (r_a - \mathcal{R}_a)(r_b - \mathcal{R}_b) \right\rangle_{\text{MD}} = 0, \quad (\text{A12})$$

and consequently Eq. (26).

### 1. The TDEP fit

Here, the equivalence of the TDEP definition in Eq. (26) with the fit procedure of the potential energy surface (Eq. 28) is demonstrated. The condition minimizing Eq. (28) is

$$\frac{\partial \mathcal{L}}{\partial \mathcal{R}_a} = - \sum_{bc} \Phi_{ab} \Phi_{bc} \langle r_c - \mathcal{R}_c \rangle_{\text{MD}} = 0, \quad (\text{A13})$$

from which we get the Eq. (25):

$$\langle r_a \rangle_{\text{MD}} = \mathcal{R}_a. \quad (\text{A14})$$

The equation for  $\Phi^{(T)}$  is a bit more involved:

$$\frac{\partial \mathcal{L}}{\partial \Phi_{cd}^{(T)}} = 2 \left\langle \left[ f_c + \sum_b \Phi_{cb}^{(T)} (r_b - \mathcal{R}_b) \right] (r_d - \mathcal{R}_d) \right\rangle_{\text{MD}} = 0 \quad (\text{A15})$$

$$\sum_b \Phi_{cb}^{(T)} \left\langle (r_b - \mathcal{R}_b)(r_d - \mathcal{R}_d) \right\rangle_{\text{MD}} = - \left\langle f_c (r_d - \mathcal{R}_d) \right\rangle_{\text{MD}} \quad (\text{A16})$$

$$\sum_b \Phi_{cb}^{(T)} \left\langle (r_b - \mathcal{R}_b)(r_d - \mathcal{R}_d) \right\rangle_{\text{MD}} = \int dr (r_d - \mathcal{R}_d) \frac{\partial V}{\partial r_c} e^{-\beta V} / Z. \quad (\text{A17})$$

Integrating by parts the last term, we get

$$- \left\langle f_c (r_d - \mathcal{R}_d) \right\rangle_{\text{MD}} = k_B T \delta_{cd}. \quad (\text{A18})$$

This is a particular case of the generalized equipartition theorem, stating

$$\left\langle \frac{\partial H}{\partial q_k} q_h \right\rangle_{\text{MD}} = \delta_{hk} k_B T,$$

where,  $q_k$  and  $q_h$  are two canonical variables, and  $H$  is the real Hamiltonian of the system. With this equality, we get

$$\sum_b \Phi_{cb}^{(T)} \left\langle (r_b - \mathcal{R}_b)(r_d - \mathcal{R}_d) \right\rangle_{\text{MD}} = k_B T \delta_{cd} \quad (\text{A19})$$

Which is satisfied by the expression of  $\Phi^{(T)}$  that maximizes the TDEP free energy (Eq. 26).

### Appendix B: Static fluctuation-dissipation theorem

Here, we report the proof of the textbook fluctuation-dissipation theorem in the static limit and discuss why it can be applied to TDEP but not to the SSCHA.

Consider a uniform force  $\xi$  perturbing the system. The new equilibrium state solves the modified Hamiltonian

$$H'(\xi) = H - \sum_b \xi_b (r_b - \mathcal{R}_b). \quad (\text{B1})$$

The new average position of the  $a$ -th atom is

$$\langle r_a \rangle_{H'(\xi)} = \frac{\int d^{3N} r d^{3N} p e^{-\beta [H - \sum_b \xi_b (r_b - \mathcal{R}_b)]} r_a}{\int d^{3N} r d^{3N} p e^{-\beta [H - \sum_b \xi_b (r_b - \mathcal{R}_b)]}} \quad (\text{B2})$$

The static response function is the derivative of the new average position with respect to the external force.

$$\frac{\partial \langle r_a - \mathcal{R}_a \rangle_{H'(\boldsymbol{\xi})}}{\partial \xi_b} = \beta \left\langle (r_b - \mathcal{R}_b)(r_a - \mathcal{R}_a) \right\rangle_{\text{MD}}. \quad (\text{B3})$$

This is no longer true if  $H$  is self-consistent like in the SSCHA, as we have to add an extra term in the derivative due to the derivative of the unperturbed Hamiltonian with respect to the new perturbed equilibrium state. This extra term gives rise to the complex system of linear equations reported in Eq. (39) and (40), derived in Appendix C.

### Appendix C: SCHA static linear response

Here, the static linear response for the SSCHA theory is obtained. The derivation follows the derivation performed for the full dynamical linear response presented in ref.[30] and coincides with the final result presented in ref.[28]. Let us compute the derivative

$$\frac{\partial \langle f_a \rangle_{\mathcal{R}, \Phi}^{(s), (s)}}{\partial \xi_b} = \int d^{3N} \mathbf{R} \frac{\partial \rho_{\mathcal{R}, \Phi}^{(s), (s)}}{\partial \xi_b} f_a(\mathbf{R}), \quad (\text{C1})$$

where  $\rho_{\mathcal{R}, \Phi}^{(s), (s)}(\mathbf{R})$  is the SCHA probability density of the SCHA. The derivative of the density with respect to the Lagrange parameter  $\xi_b$  can be obtained by using the chain rule on the two variational parameters of the SCHA:  $\mathcal{R}$  and  $\Phi$ .

For brevity, the explicit indexing of  $\mathcal{R}$  and  $\Phi$  in  $\rho$  is avoided in the rest of this appendix. The derivative of the density with respect to

$$\frac{\partial \rho}{\partial \xi_b} = \sum_h \frac{\partial \rho}{\partial \mathcal{R}_h} \frac{\partial \mathcal{R}_h}{\partial \xi_b} + \sum_{hk} \frac{\partial \rho}{\partial \Phi_{hk}} \frac{\partial \Phi_{hk}}{\partial \xi_b}, \quad (\text{C2})$$

and

$$\frac{\partial \rho}{\partial \mathcal{R}_h} = -\rho(\mathbf{R}) \sum_k \Upsilon_{hk} (R_k - \mathcal{R}_k), \quad (\text{C3})$$

$$\frac{\partial \rho}{\partial \Phi_{hk}} = \frac{\rho(\mathbf{R})}{2} \sum_{lm} \frac{\partial \Upsilon_{lm}}{\partial \Phi_{hk}} \left[ \Upsilon_{lm}^{-1} - (R_l - \mathcal{R}_l)(R_m - \mathcal{R}_m) \right], \quad (\text{C4})$$

where the  $\Upsilon$  matrix is the inverse of the covariance matrix

$$(\Upsilon^{-1})_{ab} = \left\langle (R_a - \mathcal{R}_a)(R_b - \mathcal{R}_b) \right\rangle, \quad (\text{C5})$$

in the classical limit, it becomes:

$$\Upsilon_{ab} = \frac{\Phi_{ab}}{k_B T}, \quad (\text{C6})$$

which is the classical counterpart of the quantum equation usually reported in the SSCHA papers[14, 28]:

$$\Upsilon_{ab} = \sqrt{m_a m_b} \sum_{\mu} \frac{2\omega_{\mu}}{\hbar(2n_{\mu} + 1)} e_{\mu}^a e_{\mu}^b, \quad (\text{C7})$$

where  $\omega_{\mu}$  are SCHA frequencies (square root eigenvalues of the mass rescaled  $\Phi^{(s)}$  matrix),  $e_{\mu}^a$  is the  $a$ -th Cartesian component of the  $\mu$ -th eigenvector, and  $n_{\mu}$  the corresponding Bose-Einstein occupation factor. Exploiting these relationships, we get

$$\begin{aligned} \frac{\partial \langle f_a \rangle}{\partial \xi_b} &= \sum_{hkl} \Upsilon_{kl} \left\langle (R_l - \mathcal{R}_l) f_a \right\rangle \frac{\partial \mathcal{R}_h}{\partial \xi_b} + \\ &- \frac{1}{2} \sum_{lm} \frac{\partial \Upsilon_{lm}}{\partial \Phi_{hk}} \left\langle (R_l - \mathcal{R}_l)(R_m - \mathcal{R}_m) f_a \right\rangle \frac{\partial \Phi_{lm}}{\partial \xi_b}. \end{aligned} \quad (\text{C8})$$

To obtain the other response function, we must exploit the self-consistent equation of the SCHA

$$\Phi_{ab}^{(s)} = \left\langle \frac{\partial^2 V}{\partial R_a \partial R_b} \right\rangle. \quad (\text{C9})$$

We can directly integrate this by parts to get

$$\Phi_{ab}^{(s)} = - \sum_h \Upsilon_{ah} \left\langle (R_h - \mathcal{R}_h) f_b \right\rangle, \quad (\text{C10})$$

and differentiate. Notably, the explicit derivative of  $\mathcal{R}$  in the average is zero, as it gives an average of forces that is zero at equilibrium. Thus, the only remaining derivatives are the one in  $\Upsilon$  and the one in the distribution  $\rho$



$$\begin{aligned}
\frac{\partial \Phi_{ab}^{(S)}}{\partial \xi_c} &= - \sum_{hkl} \frac{\partial \Upsilon_{ah}}{\partial \Phi_{kl}^{(S)}} \frac{\partial \Phi_{kl}^{(S)}}{\partial \xi_c} \left\langle (R_h - \mathcal{R}_h) f_b \right\rangle + \\
&+ \sum_{khl} \Upsilon_{ah} \Upsilon_{kl} \left\langle (R_h - \mathcal{R}_h)(R_l - \mathcal{R}_l) f_b \right\rangle \frac{\partial \mathcal{R}_k^{(S)}}{\partial \xi_b} + \\
&+ \frac{1}{2} \sum_{hklmn} \frac{\partial \Upsilon_{kl}}{\partial \Phi_{mn}^{(S)}} \Upsilon_{ah} \left\langle (R_h - \mathcal{R}_h)(R_k - \mathcal{R}_k)(R_l - \mathcal{R}_l) f_b \right\rangle \frac{\partial \Phi_{mn}^{(S)}}{\partial \xi_b} + \\
&- \frac{1}{2} \sum_{hklmn} \frac{\partial \Upsilon_{kl}}{\partial \Phi_{mn}^{(S)}} \Upsilon_{kl}^{-1} \Upsilon_{ha} \left\langle (R_h - \mathcal{R}_h) f_b \right\rangle \frac{\partial \Phi_{mn}^{(S)}}{\partial \xi_b}. \tag{C11}
\end{aligned}$$

We can remove the SCHA harmonic force from  $\mathbf{f}$ . This term is zero for all averages except the one multiplied by the displacement three times:

$$\begin{aligned}
\left\langle u_a u_b u_c \left( - \sum_e \Phi_{de} u_e \right) \right\rangle &= - \sum_e \Phi_{de} \left( \Upsilon_{ab}^{-1} \Upsilon_{ce}^{-1} + \right. \\
&+ \Upsilon_{ac}^{-1} \Upsilon_{be}^{-1} + \left. \Upsilon_{ae}^{-1} \Upsilon_{bc}^{-1} \right), \tag{C12}
\end{aligned}$$

where  $u_a = R_a - \mathcal{R}_a$ . Now, a bit of algebraic manipulations of matrices results in

$$\frac{\partial \Upsilon_{ab}}{\partial \Phi_{lm}^{(S)}} = \sum_{hk} \frac{\partial \Upsilon_{hk}^{-1}}{\partial \Phi_{lm}^{(S)}} \frac{\partial \Upsilon_{ab}}{\partial \Upsilon_{hk}^{-1}}, \tag{C13}$$

$$\frac{\partial \Upsilon_{ah}}{\partial \Upsilon_{pq}^{-1}} = - \Upsilon_{ap} \Upsilon_{qh}, \tag{C14}$$

$$\frac{\partial \Upsilon_{ab}}{\partial \Phi_{lm}^{(S)}} = - \sum_{hk} \frac{\partial \Upsilon_{hk}^{-1}}{\partial \Phi_{lm}^{(S)}} \Upsilon_{ah} \Upsilon_{kb}. \tag{C15}$$

The last derivative is the so-called  $\Lambda$  matrix, related to the two-phonon propagator introduced by Bianco et al. [28].

$$\frac{\partial \Upsilon_{ab}^{-1}}{\partial \Phi_{lm}^{(S)}} = 2\Lambda_{ablm}, \tag{C16}$$

and the three and four-phonon scattering vertices

$$\Phi_{abc}^{(3)} = \left\langle \frac{d^3 V}{dR_a dR_b dR_c} \right\rangle \tag{C17}$$

$$\Phi_{abcd}^{(4)} = \left\langle \frac{d^4 V}{dR_a dR_b dR_c dR_d} \right\rangle \tag{C18}$$

Coupling all together, we get the final system

$$\delta_{ab} = - \sum_h \Phi_{ah}^{(S)} \frac{\partial \mathcal{R}_h}{\partial \xi_b} + \sum_{pqlm} \Lambda_{pqlm} \Phi_{pqa}^{(3)} \frac{\partial \Phi_{lm}^{(S)}}{\partial \xi_b} \tag{C19}$$

$$\frac{\partial \Phi_{ab}^{(S)}}{\partial \xi_c} = - \sum_h \Phi_{abh}^{(3)} \frac{\partial \mathcal{R}_h}{\partial \xi_c} - \sum_{pqlm} \Lambda_{pqlm} \Phi_{pqab}^{(4)} \frac{\partial \Phi_{lm}^{(S)}}{\partial \xi_c} \tag{C20}$$

#### Appendix D: Perturbative expression of the free energy

Here, we derive the perturbative expression for the free energy and show that its diagrammatic representation coincides with the one reported in FIG. 2.

The expression of the free energy is given by

$$F = - \frac{1}{\beta} \ln Z \tag{D1}$$

$$Z = \int d^{3N} p e^{-\beta \frac{p^2}{2m}} \int d^{3N} R e^{-\beta V(R)} \tag{D2}$$

Expanding perturbatively around a small third-order term, we get

$$V(\mathbf{R}) = \frac{1}{2} \sum_{ab} \Phi_{ab} u_a u_b + \sum_{abc} \frac{1}{6} \Phi_{abc}^{(3)} u_a u_b u_c \tag{D3}$$

where  $\mathbf{u}$  represents the displacement from the average position. Perturbatively, we can expand the exponential as

$$\begin{aligned}
e^{-\beta V(R)} &\approx e^{-\frac{\beta}{2} \sum_{ab} \Phi_{ab} u_a u_b} \left( 1 - \frac{\beta}{6} \sum_{abc} \Phi_{abc}^{(3)} u_a u_b u_c + \right. \\
&\left. \frac{\beta^2}{2 \cdot 6^2} \sum_{\substack{abc \\ def}} \Phi_{abc}^{(3)} u_a u_b u_c u_d u_e u_f \Phi_{def}^{(3)} \right) \tag{D4}
\end{aligned}$$



Then we get

$$Z = Z_0 + Z_1$$

$$\frac{Z_1}{Z_0} = \frac{\beta^2}{2 \cdot 6^2} \sum_{\substack{abc \\ def}}^{(3)} \Phi_{abc} \langle u_a u_b u_c u_d u_e u_f \rangle_0 \Phi_{def}^{(3)} \quad (\text{D5})$$

where  $Z_0$  is the harmonic partition function, and the average  $\langle \cdot \rangle_0$  is performed on the harmonic Gaussian distribution. The odd term in Eq. (D4) vanishes in when averaged over a Gaussian distribution as it is the integral of an odd function ( $u^3$ ) times an even function (the Gaussian). The full free energy is

$$F \approx -\frac{1}{\beta} \ln \left[ Z_0 \left( 1 + \frac{Z_1}{Z_0} \right) \right] = F_{\text{harm}} - \frac{1}{\beta} \frac{Z_1}{Z_0} \quad (\text{D6})$$

Therefore, the correction in Eq. (D5) represents the perturbative correction beyond harmonic to the free energy, which is quadratic in the third-order term. The six-body correlation function  $\langle u_a u_b u_c u_d u_e u_f \rangle_0$  can be evaluated by exploiting the properties of Gaussian integrals by splitting it in all the possible contractions of two-body correlations:

$$\begin{aligned} \langle u_a u_b u_c u_d u_e u_f \rangle_0 &= \langle u_a u_b \rangle_0 \langle u_c u_d \rangle_0 \langle u_e u_f \rangle_0 + \\ &\quad \langle u_a u_b \rangle_0 \langle u_c u_e \rangle_0 \langle u_d u_f \rangle_0 + \\ &\quad \langle u_a u_b \rangle_0 \langle u_c u_f \rangle_0 \langle u_d u_e \rangle_0 + \dots \quad (\text{D7}) \end{aligned}$$

Each contraction is equal to the covariance matrix

$$\langle u_a u_b \rangle_0 = (\boldsymbol{\Upsilon}^{-1})_{ab}. \quad (\text{D8})$$

Exploiting the language from many-body theory,  $\langle u_a u_b \rangle_0$  is a static correlation function between two positions, i.e., the same time phononic Green function. In the language of Feynman diagrams, each one of the terms in Eq. (D7) can be represented by a line connecting two atoms  $a$  and  $b$ , while the three-phonon vertex  $\Phi_{abc}^{(3)}$  as a triangle with the three atoms  $a, b, c$  as vertices. Therefore, the expression of the free energy correction in Eq. (D5) can be written as two different terms:

$$\sum_{\substack{abc \\ def}}^{(3)} \Phi_{abc} \langle u_a u_b \rangle_0 \langle u_c u_d \rangle_0 \langle u_e u_f \rangle_0 \Phi_{def}^{(3)}, \quad (\text{D9})$$

$$\sum_{\substack{abc \\ def}}^{(3)} \Phi_{abc} \langle u_a u_d \rangle_0 \langle u_b u_e \rangle_0 \langle u_c u_f \rangle_0 \Phi_{def}^{(3)}. \quad (\text{D10})$$

All other terms in Eq. (D7) can be recast in one of Eq. (D9) and Eq. (D10) by changing the names of the labels in the summation. Eq. (D9) two indices of each three-phonons vertex are completely contracted with a phonon Green-function, leading to the Feynman diagram in FIG. 2a. Eq. (D10), on the opposite, has all phonon Green's functions connecting different three-phonons vertices, and can be depicted as FIG. 2b.

- 
- [1] U. Aseginolaza, R. Bianco, L. Monacelli, L. Paulatto, M. Calandra, F. Mauri, A. Bergara, and I. Errea, "Phonon collapse and second-order phase transition in thermoelectric SnSe," *Physical Review Letters*, vol. 122, no. 7, p. 075901, 2019.
  - [2] P. K. Schelling, S. R. Phillpot, and P. Keblinski, "Comparison of atomic-level simulation methods for computing thermal conductivity," *Phys. Rev. B*, vol. 65, p. 144306, 2002.
  - [3] A. Tenenbaum, G. Ciccotti, and R. Gallico, "Stationary nonequilibrium states by molecular dynamics. fourier's law," *Phys. Rev. A*, vol. 25, pp. 2778–2787, 1982.
  - [4] E. Drigo, M. G. Izzo, and S. Baroni, "Heat conductivity from energy-density fluctuations," *The Journal of Chemical Physics*, vol. 159, no. 18, p. 184107, 2023.
  - [5] M. Simoncelli, N. Marzari, and F. Mauri, "Unified theory of thermal transport in crystals and glasses," *Nature Physics*, vol. 15, no. 8, pp. 809–813, 2019.
  - [6] M. Born and T. von Karman *Phys. Z.*, vol. 13, p. 297, 1912.
  - [7] M. L. Klein and G. K. Horton, "The rise of self-consistent phonon theory," *Journal of Low Temperature Physics*, vol. 9, no. 3–4, p. 151, 1972.
  - [8] P. Souvatzis, O. Eriksson, M. I. Katsnelson, and S. P. Rudin, "Entropy driven stabilization of energetically unstable crystal structures explained from first principles theory," *Phys. Rev. Lett.*, vol. 100, p. 095901, 2008.
  - [9] A. van Roekeghem, J. Carrete, and N. Mingo, "Quantum self-consistent ab-initio lattice dynamics," *Computer Physics Communications*, vol. 263, p. 107945, 2021.
  - [10] D. B. Zhang, T. Sun, and R. M. Wentzcovitch, "Phonon quasiparticles and anharmonic free energy in complex systems," *Physical review letters*, vol. 112, no. 5, p. 058501, 2014.
  - [11] B. Monserrat, N. D. Drummond, and R. J. Needs, "Anharmonic vibrational properties in periodic systems: energy, electron-phonon coupling, and stress," *Physical Review B*, vol. 87, no. 14, 2013.
  - [12] I. Errea, B. Rousseau, and A. Bergara, "Isotope effect in the superconducting high-pressure simple cubic phase of calcium from first principles," *Journal of Applied Physics*, vol. 111, no. 11, p. 112604, 2012.
  - [13] I. Errea, M. Calandra, and F. Mauri, "Anharmonic free energies and phonon dispersions from the stochastic self-consistent harmonic approximation: Application to platinum and palladium hydrides," *Physical Review B*,

- vol. 89, no. 6, p. 064302, 2014.
- [14] L. Monacelli, R. Bianco, M. Cherubini, M. Calandra, I. Errea, and F. Mauri, “The stochastic self-consistent harmonic approximation: calculating vibrational properties of materials with full quantum and anharmonic effects,” *Journal of Physics: Condensed Matter*, vol. 33, no. 36, p. 363001, 2021.
- [15] T. Tadano and S. Tsuneyuki, “Self-consistent phonon calculations of lattice dynamical properties in cubic SrTiO<sub>3</sub> with first-principles anharmonic force constants,” *Physical Review B*, vol. 92, no. 5, p. 054301, 2015.
- [16] O. Hellman, I. A. Abrikosov, and S. I. Simak, “Lattice dynamics of anharmonic solids from first principles,” *Physical Review B*, vol. 84, no. 18, p. 180301, 2011.
- [17] O. Hellman and I. A. Abrikosov, “Temperature-dependent effective third-order interatomic force constants from first principles,” *Physical Review B*, vol. 88, no. 14, p. 144301, 2013.
- [18] O. Hellman and I. A. Abrikosov, “Temperature-dependent effective third-order interatomic force constants from first principles,” *Physical Review B*, vol. 88, no. 14, p. 144301, 2013.
- [19] G. Caldarelli, M. Simoncelli, N. Marzari, F. Mauri, and L. Benfatto, “Many-body green’s function approach to lattice thermal transport,” *Physical Review B*, vol. 106, no. 2, p. 024312, 2022.
- [20] D. Dangic, O. Hellman, S. Fahy, and I. Savić, “The origin of the lattice thermal conductivity enhancement at the ferroelectric phase transition in GeTe,” *npj Computational Materials*, vol. 7, no. 1, pp. 1–8, 2021.
- [21] D. Dangic, L. Monacelli, R. Bianco, F. Mauri, and I. Errea, “Large impact of phonon lineshapes on the superconductivity of solid hydrogen,” *Communications Physics*, vol. 7, no. 1, p. 150, 2024.
- [22] E. Fransson, P. Rosander, F. Eriksson, J. M. Rahm, T. Tadano, and P. Erhart, “Limits of the phonon quasiparticle picture at the cubic-to-tetragonal phase transition in halide perovskites,” *Communications Physics*, vol. 6, no. 1, p. 173, 2023.
- [23] O. Hellman, P. Steneteg, I. A. Abrikosov, and S. I. Simak, “Temperature dependent effective potential method for accurate free energy calculations of solids,” *Physical Review B*, vol. 87, no. 10, p. 104111, 2013.
- [24] T. Tadano, Y. Gohda, and S. Tsuneyuki, “Anharmonic force constants extracted from first-principles molecular dynamics: applications to heat transfer simulations,” *Journal of Physics: Condensed Matter*, vol. 26, no. 22, p. 225402, 2014.
- [25] M. Borinaga, P. Riego, A. Leonardo, M. Calandra, F. Mauri, A. Bergara, and I. Errea, “Anharmonic enhancement of superconductivity in metallic molecular-Cmca - 4 hydrogen at high pressure: a first-principles study,” *Journal of Physics: Condensed Matter*, vol. 28, no. 49, p. 494001. Publisher: IOP Publishing.
- [26] M. Borinaga, I. Errea, M. Calandra, F. Mauri, and A. Bergara, “Anharmonic effects in atomic hydrogen: Superconductivity and lattice dynamical stability,” *Physical Review B*, vol. 93, no. 17, p. 174308. Number of pages: 8 Publisher: American Physical Society.
- [27] V. V. Goldman, G. K. Horton, and M. L. Klein, “Phonon energies and lifetimes in solid ne and he in the first-order self-consistent approximation,” *Physical Review Letters*, vol. 24, pp. 1424–1427, 1970.
- [28] R. Bianco, I. Errea, L. Paulatto, M. Calandra, and F. Mauri, “Second-order structural phase transitions, free energy curvature, and temperature-dependent anharmonic phonons in the self-consistent harmonic approximation: Theory and stochastic implementation,” *Physical Review B*, vol. 96, no. 1, p. 014111, 2017.
- [29] J.-M. Lihm and C.-H. Park, “Gaussian time-dependent variational principle for the finite-temperature anharmonic lattice dynamics,” *Physical Review Research*, vol. 3, p. L032017, 2021.
- [30] L. Monacelli and F. Mauri, “Time-dependent self-consistent harmonic approximation: Anharmonic nuclear quantum dynamics and time correlation functions,” *Physical Review B*, vol. 103, no. 10, p. 104305, 2021.
- [31] A. Castellano, J. P. A. Batista, and M. J. Verstraete, “Mode-coupling theory of lattice dynamics for classical and quantum crystals,” *The Journal of Chemical Physics*, vol. 159, no. 23, p. 234501, 2023.
- [32] U. Aseginolaza, J. Diego, T. Cea, R. Bianco, L. Monacelli, F. Libbi, M. Calandra, A. Bergara, F. Mauri, and I. Errea, “Bending rigidity, sound propagation and ripples in flat graphene,” *Nature Physics*, 2024.
- [33] F. Bottin, J. Bieder, and J. Bouchet, “a-TDEP: Temperature dependent effective potential for abinit – lattice dynamic properties including anharmonicity,” *Computer Physics Communications*, vol. 254, p. 107301, 2020.
- [34] A. Siciliano, L. Monacelli, G. Caldarelli, and F. Mauri, “Wigner gaussian dynamics: Simulating the anharmonic and quantum ionic motion,” *Physical Review B*, vol. 107, no. 17, p. 174307, 2023.
- [35] D. Dangić, S. Fahy, and I. Savić, “Molecular dynamics simulation of the ferroelectric phase transition in gete: Displacive or order-disorder character,” *Physical Review B*, vol. 106, p. 134113, 2022.
- [36] T. R. Koehler, “Theoretical temperature-dependent phonon spectra of solid neon,” *Physical Review Letters*, vol. 22, p. 777, 1969.
- [37] Y. Oba, T. Tadano, R. Akashi, and S. Tsuneyuki, “First-principles study of phonon anharmonicity and negative thermal expansion in scf<sub>3</sub>,” *Physical Review Materials*, vol. 3, p. 033601, 2019.
- [38] R. Masuki, T. Nomoto, R. Arita, and T. Tadano, “Ab initio structural optimization at finite temperatures based on anharmonic phonon theory: Application to the structural phase transitions of batio<sub>3</sub>,” *Physical Review B*, vol. 106, p. 224104, 2022.
- [39] L. Monacelli, I. Errea, M. Calandra, and F. Mauri, “Black metal hydrogen above 360 GPa driven by proton quantum fluctuations,” *Nature Physics*, vol. 17, no. 1, pp. 63–67, 2021.
- [40] M. Cherubini, L. Monacelli, and F. Mauri, “The microscopic origin of the anomalous isotopic properties of ice relies on the strong quantum anharmonic regime of atomic vibration,” *Journal of Chemical Physics*, vol. 155, no. 18, p. 184502.
- [41] U. Ranieri, S. D. Cataldo, M. Rescigno, L. Monacelli, R. Gaal, M. Santoro, L. Andriambariarijaona, P. Parisiades, C. D. Michele, and L. E. Bove, “Observation of the most h<sub>2</sub>-dense filled ice under high pressure,” *Proceedings of the National Academy of Sciences*, vol. 120, no. 52, p. e2312665120, 2023.